Analytical Procedure for the Extraction of Material Parameters in Antiferroelectric ZrO_2

Mattia Segatto, *Graduate Student Member, IEEE*, Filippo Rupil, and David Esseni, *Fellow, IEEE*

***Abstract*— Here, we present an analytical procedure to extract the anisotropy constants of antiferroelectric (AFE) materials from a few key features of the experimental polarization versus field curves. Our approach is validated for two experimental datasets of ZrO_2 capacitors, and the extracted parameters are consistent with the microscopically nonpolar nature of the zero-field state of the AFE ZrO_2. The methodology has applications in AFE nonvolatile memories and memristors, as well as in electron devices exploiting the negative capacitance (NC) operation of ZrO_2.**

***Index Terms*— Antiferroelectricity, ferroelectricity, negative capacitance (NC), zirconium oxide.**

I. Introduction

ANTIFERROELECTRIC (AFE) materials are already employed in a wide range of applications, such as energy storage capacitors, electrical actuators, and nonvolatile memories [1]. In fact, AFE materials promise a few advantages over ferroelectric (FE) materials for memory applications. For example, FE hafnium oxides have a high coercive field that tends to reduce the cycling endurance [2], [3], [4], [5]. AFE materials, instead, have shown better endurance properties [6], that have been attributed to a smaller electrical stress due to the fact that one of the two memory states is nonpolar [5], to a lower charge injection [7], as well as to different switching mechanisms [7], [8].

In most perovskites, such as $PbZrO_3$, antiferroelectricity has been ascribed to a macroscopically nonpolar ground state stemming from the anti-polar alignment of polar domains [10], [11], which can be realigned by the application of an electric field. This is the physical picture behind the phenomenological Kittel's model of antiferroelectricity [12]. A more pragmatic compact model for AFE capacitors can be also based on the nucleation limited switching approach [13], or on the Preisach's model [14]. Recently, the AFE behavior has been also observed in hafnium- and zirconium-based materials [15], which exhibit also ferroelectricity and are of great interest due to their scalability and CMOS process compatibility. The microscopic picture behind antiferroelectricity in ZrO_2 is fundamentally different compared with $PbZrO_3$ and similar perovskites. In fact, ab initio calculations have revealed that the energy ground state of thin ZrO_2 films is tetragonal [16], which has been also confirmed by GIXRD measurements [5], [15], [17], so that at zero applied field, the material is microscopically nonpolar [16], [18]. By applying an electric field to the ZrO_2, a phase transition is induced from the nonpolar tetragonal phase to a polar orthorombic phase, which is the phase also responsible for ferroelectricity in hafnium–zirconium oxides (HZOs).

While Kittel's model gives an adequate description for AFE materials having an anti-polar alignment of the domains, it may not be suitable to describe the physical picture governing the antiferroelectricity in ZrO_2, which, as stated before, is quite different from the one observed in perovskites. In this article, we propose a procedure to extract the material parameters of the AFE ZrO_2 in the framework of the multidomain Landau, Ginzburg, Devonshire (LGD) model, that can be applied to AFE materials with microscopically nonpolar ground state, such as ZrO_2. The calibrated LGD model can reproduce fairly well both the quasi-static polarization-field curves in [9] and [17], and the transient negative capacitance (NC) behavior reported in [17]. Moreover, the parameterization of ZrO_2 is consistent with its microscopically nonpolar state at zero applied field.

This article is organized as follows. In Section II, we propose a methodology to extract the anisotropy constants of the LGD model for an AFE material with nonpolar ground state. In Section III, we provide a quick overview of the simulation framework used to validate the proposed extraction procedure. In Section IV, we show comparisons between simulations and experiments for different ZrO_2 thicknesses and operation regimes. In Section V, we offer a few concluding remarks.

II. Extraction of Anisotropy Constants

Here, let us consider a capacitor with metal electrodes and an FE or AFE dielectric (DE). For a simple homogeneous polarization picture, the Gibbs' free energy of the system consisting of the capacitor and the external battery can be

Manuscript received 7 March 2023; accepted 4 April 2023. Date of publication 18 April 2023; date of current version 25 May 2023. This work was supported in part by the European Union H2020 under Grant GA:871737. The review of this article was arranged by Editor N. Xu. *(Corresponding author: Mattia Segatto.)*

Mattia Segatto and David Esseni are with the Polytechnic Department of Engineering and Architecture (DPIA), University of Udine, 33100 Udine, Italy (e-mail: segatto.mattia@spes.uniud.it).

Filippo Rupil is with the Polytechnic Department of Engineering and Architecture (DPIA), University of Udine, 33100 Udine, Italy.

Color versions of one or more figures in this article are available at https://doi.org/10.1109/TED.2023.3265626.

Digital Object Identifier 10.1109/TED.2023.3265626

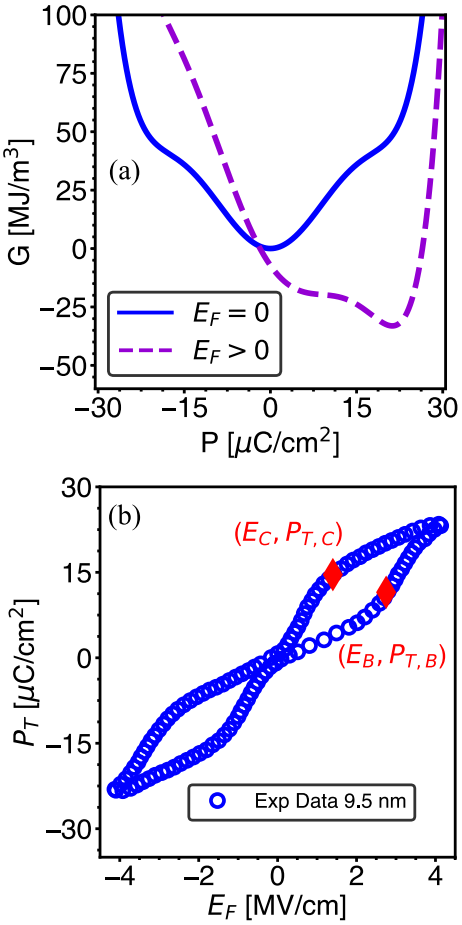

Fig. 1. (a) Gibbs' free energy landscapes calculated from (1) with the anisotropy constants in Table I, and for either a zero or a positive applied field E_F. At zero field (blue curve), the point $E_F = P = 0$ is a free energy minimum, and thus, it is a stable steady-state point for the system. The application of a positive E_F (purple curve) shifts the energy minimum to a positive P. (b) Measured total polarization versus applied electric field in a TiN/ZrO_2 (9.5 nm)/TiN stack [9]. The meaning of points B and C is discussed in the text.

written as follows [19]:

$$G = \alpha P^2 + \beta P^4 + \gamma P^6 - E_F\, P - \frac{\varepsilon_0 \varepsilon_F E_F^2}{2} \tag{1}$$

where ε_0 is the vacuum permittivity, and P, ε_F, and E_F are the spontaneous polarization, background permittivity, and electric field of the FE or AFE material, while α, β, and γ are the anisotropy constants. The quasi-static P–E_F trajectories are identified by the conditions $(dG/dP) = 0$ and $(d^2G/dP^2) > 0$, [20], namely

$$2\alpha P + 4\beta P^3 + 6\gamma P^5 = E_F \tag{2a}$$

$$\frac{\partial E_F}{\partial P} = 2\alpha + 12\beta P^2 + 30\gamma P^4 \geq 0. \tag{2b}$$

Quasi-static experiments in a metal–FE–metal or metal–AFE–metal (M–AFE–M) stack probe the overall charge in the system, usually denoted as total polarization $P_T \approx Q = P + \varepsilon_0 \varepsilon_F\, E_F$.

Fig. 1(a) shows an example of the free energy landscape for an M–AFE–M system, and (2) prescribes that α be positive in order to have a microscopically nonpolar stable state at $E_F \approx 0$ and $P \approx 0$. Fig. 1(b) displays the experimental P_T versus E_F curve recently reported for a ZrO_2 capacitor [9]. In Fig. 1(b), we denote by E_B and E_C the coercive fields corresponding, respectively, to the nonpolar to positive and positive to nonpolar transition in the P_T–E_F curve. In practice, the points $(E_B,\ P_{T,B})$ and $(E_C,\ P_{T,C})$ can be identified as the points where the P_T versus E_F curve exhibits a clear change in the slope. In order to define an analytical procedure for the extraction of material parameters in AFE ZrO_2, we now assume that points B and C correspond, respectively, to a maximum and a minimum of the static $E_F - P_T$ relation implied by the LGD polynomial. In the Appendix, we show that such maximum and minimum of the $E_F - P_T$ relation coincide with those of the $E_F - P$ relation, which, in turn, are readily identified by the condition $(\partial E_F/\partial P) = 0$ in (2b). Hence, the conditions ensuring that the quasi-static $P_T - E_F$ trajectories include points B and C become

$$52\alpha + 12\beta\, P_C^2 + 30\gamma\, P_C^4 = 0 \tag{3a}$$

$$2\alpha\, P_C + 4\beta\, P_C^3 + 6\gamma\, P_C^5 = E_C \tag{3b}$$

$$2\alpha + 12\beta\, P_B^2 + 30\gamma\, P_B^4 = 0 \tag{3c}$$

$$2\alpha\, P_B + 4\beta\, P_B^3 + 6\gamma\, P_B^5 = E_B. \tag{3d}$$

From (3a) to (3c), we can readily express α, β, and γ as follows:

$$\alpha = \frac{3}{4}\frac{E_C}{P_C} + \frac{3}{4}\frac{E_C P_C}{5P_B^2 - P_C^2} \tag{4a}$$

$$\beta = -\frac{E_C}{8P_C^3} - \frac{3}{4}\frac{E_C}{P_C\left(5P_B^2 - P_C^2\right)} \tag{4b}$$

$$\gamma = \frac{E_C}{4P_C^3\left(5P_B^2 - P_C^2\right)}. \tag{4c}$$

Equation (4) provides the anisotropy constants in terms of E_C, P_C, and P_B. However, the spontaneous polarizations P_C and P_B cannot be directly identified in the experimental curves of Fig. 1(b), but they must be calculated by using $P = P_T - \varepsilon_F \varepsilon_0\, E_F$. This implies that α, β, and γ in (4) are given in terms of E_C, $P_{T,C}$, and $P_{T,B}$ and of the remaining parameter ε_F. In this latter respect, it has been theoretically argued that ε_F should be considered an adjustable parameter rather a true material constant [21], and in practice, it is difficult to extract ε_F independently of α, β, and γ. Therefore, we now substitute α, β, and γ from (4) into (3d) and rearrange it as follows:

$$\frac{P_C^3\left(5P_B^2 - P_C^2\right)}{P_B^3\left(5P_C^2 - P_B^2\right)} = \frac{E_C}{E_B}. \tag{5}$$

By recalling $P_C = P_{T,C} - \varepsilon_0 \varepsilon_F\, E_C$ and $P_B = P_{T,B} - \varepsilon_0 \varepsilon_F\, E_B$, (5) can now be solved for ε_F. Namely, ε_F can be used as the fourth adjustable parameter determined by (3), so as to ensure that the quasi-static $P_T - E_F$ trajectories include the points B and C in Fig. 1(b).

As it can be seen, (5) implies also $(5P_B^2 - P_C^2) > 0$ (because $5P_C^2$ is by definition larger than P_B^2), which, in turn, results in positive α and γ values and in a negative β value [see (4)]. As already mentioned, the positive α value is consistent with the microscopically nonpolar nature of thin ZrO_2 films at a zero applied field, and it is also consistent with previous

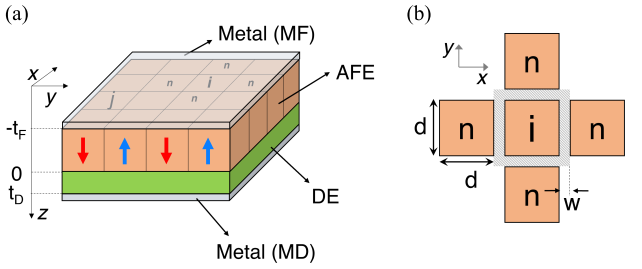

Fig. 2. Sketch of a device structure corresponding to a metal–AFE–DE–metal stack. (a) Sketch showing thickness t_F of the AFE layer, the thickness t_D of the DE, and the partition of the AFE layer in n_D domains. (b) Focus on the nearest neighbor domains included in the sum over n in (6), and describing the domain wall energy contribution. d and w denote, respectively, the domain size and the width of the domain wall region [19].

literature for AFE ZrO_2 [22], [23]. Moreover, a positive α value is the only possible choice in order to obtain no remnant polarization.

In summary, the procedure to extract the anisotropy constants from experiments requires to first identify the points B and C in the measured P_T–E_F curves [see Fig. 1(b)]. Then, (5) can be solved numerically to determine ε_F, and once ε_F is known, (4) provides expressions for α, β, and γ.

III. Framework for Numerical Modeling

In Section IV, we will illustrate several comparisons between simulations and experiments aimed at a validation of the extraction procedure for the anisotropy constants of ZrO_2. All simulations were carried out by using the solver for the multidomain LGD equations that has been already discussed in [19], [24], and [25]. In this section, we recall only a few aspects of the simulation framework, which are relevant for the cases at study in this article. For an AFE or an FE material consisting of n_D domains, as shown in Fig. 2, the dynamics of the polarization P_i in each domain is described by the following equations [19], [24], [25]:

$$\frac{\partial P_i}{\partial t} = \frac{1}{t_F\,\rho}\Bigg[-\left(2\alpha_i\,P_i + 4\beta_i\,P_i^3 + 6\gamma_i\,P_i^5\right)t_F - \frac{t_F\,k}{d\,w}\sum_n (P_i - P_n) - \sum_{j=1}^{n_D} P_j / C_{i,j}^{(\mathrm{dep})} + (C_D/C_0)V_T\Bigg] \tag{6}$$

where k is the domain wall coupling coefficient, ρ is the switching resistivity, while $1/C_{i,j}^{(\mathrm{dep})} = 1/2(1/C_{j,i} + 1/C_{i,j})$, and the terms $C_{i,j}$ are the capacitive couplings between domains. Given the similarity between the crystal chemistry of ZrO_2 and HfO_2 [26], in simulations, we used $k \approx 0$, as suggested by recent first principle calculations for HfO_2 [27]. For each domain, the α_i, β_i, and γ_i values were calculated by using a Gaussian distribution of the coercive fields with the mean E_C and E_B values used to extract the parameters in Table I and with a ratio $\sigma_{\mathrm{EC}} = \sigma_{\mathrm{EB}}$ between the standard deviation and mean value; ε_F is the same in all domains. All simulations were performed using $n_D = 400$ domains with a domain area of 25 nm^2. The number of domains n_D mainly influences the number of terms $1/C_{i,j}^{(\mathrm{dep})}$, which, as stated before, describe the capacitive coupling between the ith and jth domains. However, such a capacitive coupling decreases quite steeply with the distance between domains, so that simulations become insensitive to n_D for large enough n_D values. Moreover, for an M–AFE–M stack (without the DE layer in Fig. 2), the terms $1/C_{i,j}^{(\mathrm{dep})}$ tend to zero, because there is no electrostatic coupling between the domains through the DE layer, which further reduces the sensitivity to n_D of the simulations results. The experimental P_T versus E_F curves for AFE ZrO_2 sometimes exhibit a non-negligible polarization at zero field, that is ascribed to the presence of FE domains. Therefore, in our simulations, we accounted for a small fraction of FE domains, which can be included in our model by setting appropriate values of the anisotropy constants for such domains. More precisely, for the LGD parameterization of FE domains in ZrO_2, we used educated guesses for the remnant polarization $P_r \simeq 25\ \mu\mathrm{C/cm}^2$ and coercive field $E_{C,\mathrm{FE}} \simeq 1.2$ MV/cm consistent with [28] and [29], resulting in the following LGD parameterization: $\alpha_{\mathrm{FE}} = -5.94 \cdot 10^8$ m^3/F, $\beta_{\mathrm{FE}} = 4.28 \cdot 10^9$ $\mathrm{m}^5/(\mathrm{FC}^2)$, and $\gamma_{\mathrm{FE}} = 1.16 \cdot 10^9$ $\mathrm{m}^9/(\mathrm{FC}^4)$. Even for FE domains, we introduced a Gaussian distribution of the coercive field, with the same σ_{EC} value used for AFE domains. The domain-dependent anisotropy constants have a spatially random distribution across the domain grid, and we have verified that their spatial distribution does not practically affect the simulation results. This is not unexpected especially for M–AFE–M stacks, where there is no electrostatic coupling between the domains. In our simulations, it is also possible to include a small built-in electric field in the FE material, possibly arising from a slight work-function difference at the two electrodes or from fixed charges in the DE stack.

TABLE I
Nominal Values of the Parameters Extracted From (4) and (5) for Experiments From [9] and [17]. E_{BI} Denotes a Built-In Electric Field; the Switching Resistivity $\rho \sim 400\ \Omega\mathrm{m}$ Was Used in All Simulations

	α [m/F]	β [$\mathrm{m}^5/(\mathrm{FC}^2)$]	γ [$\mathrm{m}^9/(\mathrm{FC}^4)$]	ε_F [-]	t_{ZrO_2} [nm]	E_{BI} [kV/cm]
[9]	$3.37 \cdot 10^9$	$-1.57 \cdot 10^{11}$	$3.24 \cdot 10^{12}$	23.76	5.3	0
[9]	$3.56 \cdot 10^9$	$-2.01 \cdot 10^{11}$	$4.50 \cdot 10^{12}$	22.09	9.5	-50
[17]	$2.95 \cdot 10^9$	$-8.97 \cdot 10^{10}$	$1.09 \cdot 10^{12}$	13.36	10	50

IV. Comparison With Experimental Results

Table I reports the material parameters extracted with the methodology of this work from two experimental datasets, namely, the P_T–E_F curves recently reported in [9] and [17]. Quite interestingly, from the parameters in Table I, one can calculate the zero-field permittivity of ZrO_2, which is defined as $1/\varepsilon_0(\partial P_T/\partial E_F)$ at $E_F = P_T = 0$. By recalling $P_T = P + \varepsilon_0\varepsilon_F E_F$ and using (2a) for $(\partial P/\partial E_F)$, the zero-field permittivity is readily expressed as $(\varepsilon_F + 1/(2\alpha\varepsilon_0))$. As already mentioned in Section II, while ε_F is related to the zero-field permittivity, which is the quantity actually measured in experiments, it is not equivalent to it and can be thought as a fitting parameter [21].

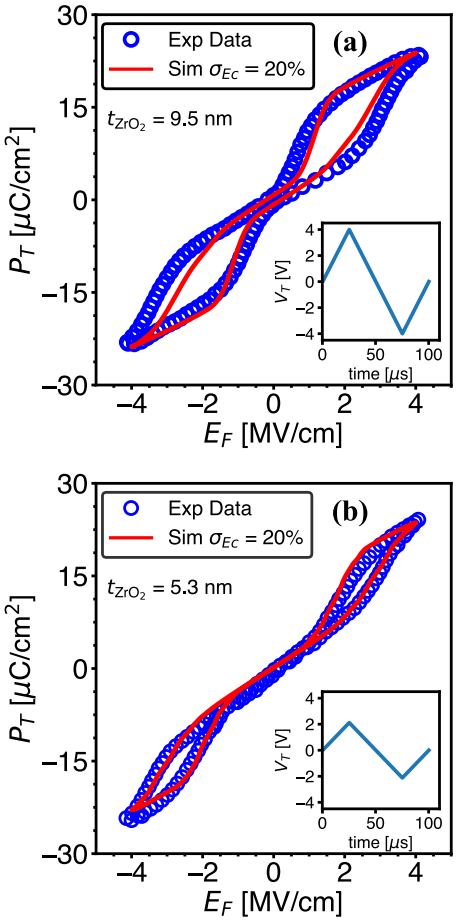

Fig. 3. Comparison between simulations and experiments for quasi-static P_T versus E_F curves of the TiN/ZrO_2/TiN capacitors from [9]. The triangular voltage waveforms at a 10-kHz frequency are shown in the insets. (a) Thickness of the ZrO_2 layer t_{ZrO_2} = 9.5 nm, points used for parameters extraction: (E_B, $P_{T,B}$) = (2.7 MV/cm, 9.5 μC/cm^2); (E_C, $P_{T,C}$) = (1.1 MV/cm, 14.5 μC/cm^2). (b) t_{ZrO_2} = 5.3 nm, (E_B, $P_{T,B}$) = (2.9 MV/cm, 14 μC/cm^2); (E_C, $P_{T,C}$) = (2.4 MV/cm, 16 μC/cm^2).

The zero-field permittivity obtained from the parameters in Table I ranges between 30 and 40, which is in good agreement with experimental values in [30] and [31]. The anisotropy constants in Table I provide the mean values of the domain-dependent α_i, β_i, and γ_i parameters used in the numerical simulations.

In Fig. 3, we show a comparison between simulations and experiments for the P_T–E_F curves of the M–AFE–M stacks reported in [9] and for the materials parameters in Table I. In Fig. 3(a), we considered 3% of the overall domains to be FE with the parameters discussed in Section III, while for Fig. 3(b), we did not include FE domains, as it can be seen that the hysteresis of the P_T–E_F curve is completely closed at zero applied electric field.

In our model, the timescale for the polarization dynamics is $t_\rho = \rho/(2\langle\alpha\rangle)$ [24]. For $\rho \approx 400\ \Omega$ m (see Table I), we have $t_\rho \approx 70$ ns, which is consistent with the literature for large-area devices [32] and ensures that simulations in Fig. 3 are quasi-static. While it could be argued that each stack could have its own ρ value, there is no direct measurement to extract it, rather it is usually inferred from polarization switching

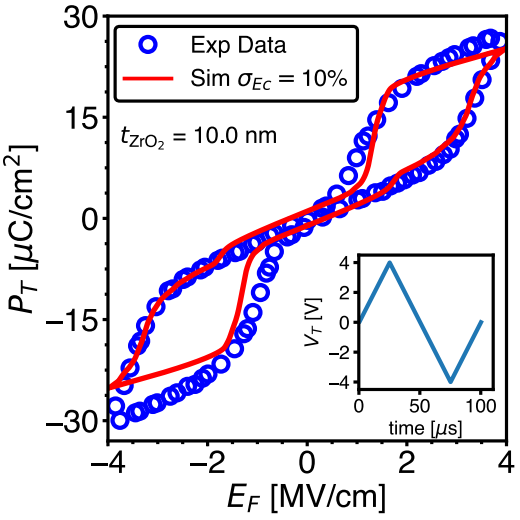

Fig. 4. Comparison between simulations and experiments for quasi-static P_T versus E_F curves of a TiN/ZrO_2/TiN capacitor from [17]. The triangular voltage waveforms at a 10-kHz frequency are shown in the inset. (E_B, $P_{T,B}$) = (3.1 MV/cm, 12 μC/cm^2); (E_C, $P_{T,C}$) = (1.6 MV/cm, 18 μC/cm^2).

measurements [33]. Given the lack of a direct information about the value of ρ, we kept its value fixed for all stacks. The agreement between simulations and experiments is fairly good for both t_{ZrO_2} values because of a good symmetry of the experiments along both the P_T and E_F axes.

Fig. 4 reports a similar comparison for the experimental dataset in [17], where we considered 4% of the domains to be FE. The agreement between simulations and experiments is still fairly good, but we also observe a discrepancy in the negative E_F hysteresis. This is mainly due to an asymmetry in the measured P_T values for positive and negative E_F at large $|E_F|$, possibly due to a non-negligible influence of leakage. In fact, while an asymmetry along the E_F axis can be included in our model through a built-in field E_{BI} (see Table I), the LGD model is instead inherently symmetric in the P_T values.

Hoffmann et al. [17] also reported transient NC experiments, that we here analyze by using the LGD model, as previously reported for the NC behavior in FE devices [24], [34], [35], [36]. In the TiN/ZrO_2/Al_2O_3/HfO_2/TiN stack, the undoped HfO_2 layer is paraelectric, and the thicknesses are as follows: $t_{ZrO_2} = 10$ nm, $t_{Al_2O_3} \approx 1$ nm, and $t_{HfO_2} = 8$ nm. The timescale of the voltage pulses in these experiments (now comparable to the t_ρ), and the relatively thick DE were on purposely chosen to minimize the role of charge injection and trapping [17]. Therefore, our simulations neglect trapping, which has been shown to be instead important in quasi-static measurements for FE-oxide stacks having a thin DE layer [25], [37]. Fig. 5(a) and (c) compares the simulated and experimental P_T–V_{max} curves for a pulse width of, respectively, 275 ns and 1 μs, where V_{max} is the amplitude of the voltage pulse, and the simulated P_T values have been extracted following the definition in [17]. Fig. 5(b) and (d) displays the corresponding plots for the P_T versus an effective electric field, E_{EFF}, across the ZrO_2 layer. In experiments, the E_{EFF} cannot be directly probed; hence, it was estimated as $E_{EFF} \approx (V_{max} - P_T/C_D)/t_{ZrO_2}$, where $C_D \approx 1.78\ \mu$F/cm^2 is the effective

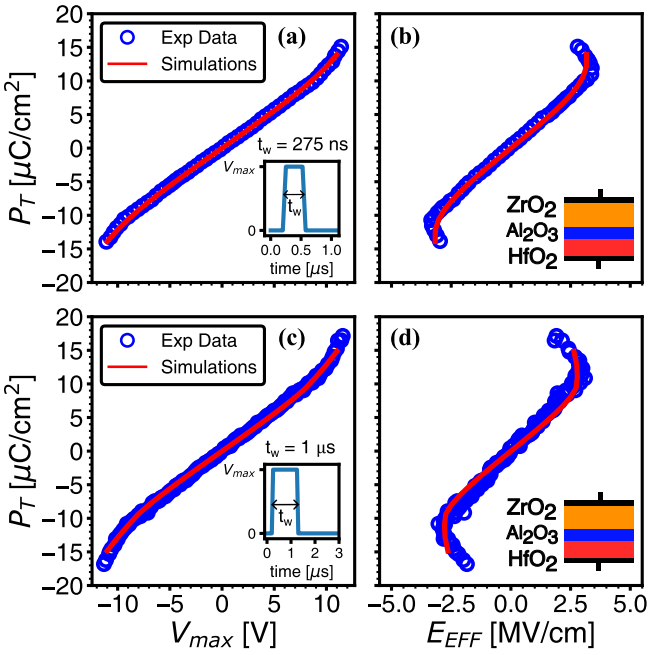

Fig. 5. Comparison between simulations and experiments for transient NC measurements in a TiN/ZrO_2/Al_2O_3/HfO_2/TiN capacitor [17]. (a) and (c) P_T versus V_{max} curve for pulsed measurements with a pulsewidth of 275 ns and 1 μs, respecitvely. (b) and (d) Corresponding P_T versus effective field, E_{EFF}, curve.

capacitance of the Al_2O_3–HfO_2 series [17]. In the simulations of Fig. 5(b) and (d), the E_{EFF} was calculated according to the same definition given in [17]. Fig. 5 shows that the same ZrO_2 parameters already employed in Fig. 4, both LGD mean values and their statistical distribution, can provide a fairly good agreement also for transient NC experiments, with a matching between simulations and experiments that is similarly good for the two different pulse widths. The results in Fig. 5 reinforce our confidence in the extraction procedure for the ZrO_2 parameters and in the overall simulation framework.

V. Discussion and Conclusion

We have proposed a procedure to extract the material parameters for the LGD model of AFE ZrO_2 films, which is consistent with the microscopically nonpolar nature of the zero-field state in AFE ZrO_2 [17]. The points $(E_B, P_{T,B})$ and $(E_C, P_{T,C})$ necessary to extract the anisotropy constants can be reliably identified by a distinct change in P_T versus E_F slope of the P_T–E_F curves [see Fig. 1(b)], provided that the curves are not significantly distorted by leakage and that they display a full hysteresis loop, as opposed to minor loops. Our methodology was successfully validated by considering quasi-static P_T–E_F curves in M–AFE–M stacks, where a small fraction of FE domains was also included in the model to explain and reproduce the residual polarization at zero field observed in some AFE ZrO_2 films [9]. Moreover, we analyzed very recent experiments reporting both P_T–E_F curves in M–AFE–M stacks and transient NC experiments in a TiN/ZrO_2/Al_2O_3/HfO_2/TiN stack. With a single set of ZrO_2 parameters extracted from the P_T–E_F curves, our simulations could reproduce fairly well also the transient NC experiments and for different pulse widths.

Our analytical extraction procedure has a clear physical background, and it is easy to implement, although it may lead to fitting results that are not as accurate as those obtained with more phenomenological approaches [13], [14], where the quite many parameters of the models are typically extracted by using numerical procedures targeting a minimization of the mean-squared error between simulations and experiments.

We believe that the methodology proposed in this article to extract the anisotropy constants of antiferroelectic ZrO_2 layers will have useful applications in FE nonvolatile memories and memristors, as well as in possible devices exploiting the ZrO_2 NC behavior.

Appendices

In order to show that the maximum and minimum of the static E_F–P_T curve coincide with those of the E_F–P curve, we can substitute $P = P_T - \varepsilon_0\varepsilon_F E_F$ in (2a) and obtain

$$E_F = 2\alpha(P_T - \varepsilon_0\varepsilon_F E_F) + 4\beta(P_T - \varepsilon_0\varepsilon_F E_F)^3 + 6\gamma(P_T - \varepsilon_0\varepsilon_F E_F)^5. \quad (7)$$

Then, we derive both sides of (7) with respect to P_T, and we have

$$\frac{\partial E_F}{\partial P_T} = 2\alpha\left(1 - \varepsilon_0\varepsilon_F E_F \frac{\partial E_F}{\partial P_T}\right) + 12\beta \underbrace{(P_T - \varepsilon_0\varepsilon_F E_F)^2}_{P^2}\left(1 - \varepsilon_0\varepsilon_F E_F \frac{\partial E_F}{\partial P_T}\right) + 30\gamma \underbrace{(P_T - \varepsilon_0\varepsilon_F E_F)^4}_{P^4}\left(1 - \varepsilon_0\varepsilon_F E_F \frac{\partial E_F}{\partial P_T}\right) \quad (8)$$

which can be refactored in

$$\frac{\partial E_F}{\partial P_T}\left[1 + \varepsilon_0\varepsilon_F(2\alpha + 12\beta P^2 + 30\gamma P^4)\right] = 2\alpha + 12\beta P^2 5 + 30\gamma P^4. \quad (9)$$

Equation (9) clearly shows that the condition

$$\frac{\partial E_F}{\partial P} = 2\alpha + 12\beta P^2 + 30\gamma P^4 = 0 \quad (10)$$

implies also $(\partial E_F/\partial P_T) = 0$.

Acknowledgment

The authors are thankful to Daniel Lizzit, Riccardo Fontanini, and Marco Massarotto for fruitful discussions, and to Michael Hoffmann for sharing experimental data of [17].

References

[1] C. A. Randall, Z. Fan, I. Reaney, L. Chen, and S. Trolier-McKinstry, "Antiferroelectrics: History, fundamentals, crystal chemistry, crystal structures, size effects, and applications," *J. Amer. Ceram. Soc.*, vol. 104, no. 8, pp. 3775–3810, Aug. 2021, doi: 10.1111/jace.17834.

[2] E. Yurchuk et al., "Origin of the endurance degradation in the novel HfO_2-based 1T ferroelectric non-volatile memories," in *Proc. IEEE Int. Rel. Phys. Symp.*, Jun. 2014, pp. 2E.5.1–2E.5.5.

[3] M. Pesic et al., "Root cause of degradation in novel HfO_2-based ferroelectric memories," in *Proc. IEEE Int. Rel. Phys. Symp. (IRPS)*, Apr. 2016, pp. MY-3-1–MY-3-5.

[4] M. Pesic et al., "Physical mechanisms behind the field-cycling behavior of HfO_2-based ferroelectric capacitors," *Adv. Funct. Mater.*, vol. 26, no. 25, pp. 4601–4612, 2016, doi: 10.1002/adfm.201600590.

[5] M. Pesic, M. Hoffmann, C. Richter, T. Mikolajick, and U. Schroeder, "Nonvolatile random access memory and energy storage based on antiferroelectric like hysteresis in ZrO_2," *Adv. Funct. Mater.*, vol. 26, no. 41, pp. 7486–7494, 2016, doi: 10.1002/adfm.201603182.

[6] M. H. Park, H. J. Kim, Y. J. Kim, T. Moon, K. D. Kim, and C. S. Hwang, "Thin $Hf_xZr_{1-x}O_2$ films: A new lead-free system for electrostatic supercapacitors with large energy storage density and robust thermal stability," *Adv. Energy Mater.*, vol. 4, no. 16, Nov. 2014, Art. no. 1400610, doi: 10.1002/aenm.201400610.

[7] X. J. Lou, "Why do antiferroelectrics show higher fatigue resistance than ferroelectrics under bipolar electrical cycling?" *Appl. Phys. Lett.*, vol. 94, no. 7, Feb. 2009, Art. no. 072901, doi: 10.1063/1.3082375.

[8] L. Zhou, R. Z. Zuo, G. Rixecker, A. Zimmermann, T. Utschig, and F. Aldinger, "Electric fatigue in antiferroelectric ceramics induced by bipolar electric cycling," *J. Appl. Phys.*, vol. 99, no. 4, Feb. 2006, Art. no. 044102, doi: 10.1063/1.2172725.

[9] X. Luo, K. Toprasertpong, M. Takenaka, and S. Takagi, "Antiferroelectric properties of ZrO_2 ultra-thin films prepared by atomic layer deposition," *Appl. Phys. Lett.*, vol. 118, no. 23, Jun. 2021, Art. no. 232904, doi: 10.1063/5.0051068.

[10] E. Sawaguchi, H. Maniwa, and S. Hoshino, "Antiferroelectric structure of lead zirconate," *Phys. Rev.*, vol. 83, no. 5, p. 1078, Sep. 1951, doi: 10.1103/PhysRev.83.1078.

[11] A. N. Morozovska, E. A. Eliseev, A. Biswas, N. V. Morozovsky, and S. V. Kalinin, "Effect of surface ionic screening on polarization reversal and phase diagrams in thin antiferroelectric films for information and energy storage," *Phys. Rev. Appl.*, vol. 16, no. 4, Oct. 2021, Art. no. 044053, doi: 10.1103/PhysRevApplied.16.044053.

[12] C. Kittel, "Theory of antiferroelectric crystals," *Phys. Rev.*, vol. 82, no. 5, pp. 729–732, Jun. 1951, doi: 10.1103/PhysRev.82.729.

[13] C.-T. Tung, S. Salahuddin, and C. Hu, "A compact model of antiferroelectric capacitor," *IEEE Electron Device Lett.*, vol. 43, no. 2, pp. 316–318, Feb. 2022.

[14] Z. Wang, J. Hur, N. Tasneem, W. Chern, S. Yu, and A. Khan, "Extraction of Preisach model parameters for fluorite-structure ferroelectrics and antiferroelectrics," *Sci. Rep.*, vol. 11, no. 1, p. 12474, Jun. 2021, doi: 10.1038/s41598-021-91492-w.

[15] J. Müller et al., "Ferroelectricity in simple binary ZrO_2 and HfO_2," *Nano Lett.*, vol. 12, no. 8, pp. 4318–4323, 2012, doi: 10.1021/nl302049k.

[16] S. E. Reyes-Lillo, K. F. Garrity, and K. M. Rabe, "Antiferroelectricity in thin-film ZrO_2 from first principles," *Phys. Rev. B, Condens. Matter*, vol. 90, no. 14, Oct. 2014, Art. no. 140103, doi: 10.1103/PhysRevB.90.140103.

[17] M. Hoffmann et al., "Antiferroelectric negative capacitance from a structural phase transition in zirconia," *Nature Commun.*, vol. 13, no. 1, p. 1228, Mar. 2022, doi: 10.1038/s41467-022-28860-1.

[18] S. Lombardo et al., "Atomic-scale imaging of polarization switching in an (anti-)ferroelectric memory material: Zirconia (ZrO_2)," in *Proc. IEEE Symp. VLSI Technol.*, Jun. 2020, pp. 1–2.

[19] T. Rollo, F. Blanchini, G. Giordano, R. Specogna, and D. Esseni, "Stabilization of negative capacitance in ferroelectric capacitors with and without a metal interlayer," *Nanoscale*, vol. 12, no. 10, pp. 6121–6129, 2020.

[20] T. Rollo and D. Esseni, "Energy minimization and Kirchhoff's laws in negative capacitance ferroelectric capacitors and MOSFETs," *IEEE Electron Device Lett.*, vol. 38, no. 6, pp. 814–817, Jun. 2017.

[21] A. P. Levanyuk, B. A. Strukov, and A. Cano, "Background dielectric permittivity: Material constant or fitting parameter?" *Ferroelectrics*, vol. 503, no. 1, pp. 94–103, Oct. 2016, doi: 10.1080/00150193.2016.1218245.

[22] P. D. Lomenzo, M. Materano, C. Richter, R. Alcala, T. Mikolajick, and U. Schroeder, "A Gibbs energy view of double hysteresis in ZrO_2 and Si-doped HfO_2," *Appl. Phys. Lett.*, vol. 117, no. 14, Oct. 2020, Art. no. 142904, doi: 10.1063/5.0018199.

[23] Y. Xu et al., "Improved multibit storage reliability by design of ferroelectric modulated antiferroelectric memory," *IEEE Trans. Electron Devices*, vol. 69, no. 4, pp. 2145–2150, Apr. 2022.

[24] D. Esseni and R. Fontanini, "Macroscopic and microscopic picture of negative capacitance operation in ferroelectric capacitors," *Nanoscale*, vol. 13, no. 21, pp. 9641–9650, 2021.

[25] M. Segatto, R. Fontanini, F. Driussi, D. Lizzit, and D. Esseni, "Limitations to electrical probing of spontaneous polarization in ferroelectric-dielectric heterostructures," *IEEE J. Electron Devices Soc.*, vol. 10, pp. 324–333, 2022.

[26] T. S. Böscke, J. Müller, D. Bräuhaus, U. Schröder, and U. Böttger, "Ferroelectricity in hafnium oxide thin films," *Appl. Phys. Lett.*, vol. 99, no. 10, Sep. 2011, Art. no. 102903.

[27] H.-J. Lee et al., "Scale-free ferroelectricity induced by flat phonon bands in HfO_2," *Science*, vol. 369, no. 6509, pp. 1343–1347, 2020, doi: 10.1126/science.aba0067.

[28] R. Cao et al., "Effects of capping electrode on ferroelectric properties of $Hf_{0.5}Zr_{0.5}O_2$ thin films," *IEEE Electron Device Lett.*, vol. 39, no. 8, pp. 1207–1210, Jun. 2018.

[29] B. S. Kim et al., "A comparative study on the ferroelectric performances in atomic layer deposited $Hf_{0.5}Zr_{0.5}O_2$ thin films using tetrakis(ethylmethylamino) and tetrakis(dimethylamino) precursors," *Nanosc. Res. Lett.*, vol. 15, no. 1, p. 72, Apr. 2020, doi: 10.1186/s11671-020-03301-4.

[30] K. Kato et al., "Stabilized formation of tetragonal ZrO_2 thin film with high permittivity," *Thin Solid Films*, vol. 557, pp. 192–196, Jan. 2014. [Online]. Available: https://www.sciencedirect.com/science/article/pii/S0040609014000522

[31] J. Liu, J. Li, J. Wu, and J. Sun, "Structure and dielectric property of high-k ZrO_2 films grown by atomic layer deposition using tetrakis(dimethylamido)zirconium and ozone," *Nanosc. Res. Lett.*, vol. 14, no. 1, p. 154, May 2019, doi: 10.1186/s11671-019-2989-8.

[32] M. Si et al., "Ultrafast measurements of polarization switching dynamics on ferroelectric and anti-ferroelectric hafnium zirconium oxide," *Appl. Phys. Lett.*, vol. 115, no. 7, Aug. 2019, Art. no. 072107, doi: 10.1063/1.5098786.

[33] M. Kobayashi, N. Ueyama, K. Jang, and T. Hiramoto, "Experimental study on polarization-limited operation speed of negative capacitance FET with ferroelectric HfO_2," in *IEDM Tech. Dig.*, Dec. 2016, pp. 314–317.

[34] M. Hoffmann et al., "Intrinsic nature of negative capacitance in multidomain $Hf_{0.5}Zr_{0.5}O_2$-based ferroelectric/dielectric heterostructures," *Adv. Funct. Mater.*, vol. 32, no. 2, Jan. 2022, Art. no. 2108494, doi: 10.1002/adfm.202108494

[35] A. K. Saha and S. K. Gupta, "Multi-domain negative capacitance effects in metal-ferroelectric-insulator-semiconductor/metal stacks: A phase-field simulation based study," *Sci. Rep.*, vol. 10, no. 1, p. 10207, Jun. 2020, doi: 10.1038/s41598-020-66313-1.

[36] A. K. Saha and S. K. Gupta, "Negative capacitance effects in ferroelectric heterostructures: A theoretical perspective," *J. Appl. Phys.*, vol. 129, no. 8, Feb. 2021, Art. no. 080901, doi: 10.1063/5.0038971.

[37] R. Fontanini et al., "Charge-trapping-induced compensation of the ferroelectric polarization in FTJs: Optimal conditions for a synaptic device operation," *IEEE Trans. Electron Devices*, vol. 69, no. 7, pp. 3694–3699, Jul. 2022.

Open Access funding provided by 'Università degli Studi di Udine' within the CRUI CARE Agreement